Multilevel Analysis of Nuclear Dynamics in Lamin Perturbed Fibroblasts

Winnok H. De Vos[a], Frederik Houben[b], Jos Broers[b], Ron A. Hoebe[c], Erik M.M. Manders[d], Greg Joss[e], Frans Ramaekers[b] and Patrick Van Oostveldt[a]

[a] Dept. of Molecular Biotechnology, Ghent University, Coupure links 653, 9000 Ghent, Belgium;
[b] Dept. of Molecular Cell Biology, University of Maastricht, Universiteitssingel 50, 6229 ER Maastricht, The Netherlands;
[c] Centre for Advanced Microscopy, Swammerdam Institute for Life Sciences, University of Amsterdam, Kruislaan 316, 1098 SM Amsterdam, The Netherlands;
[d] Dept. of Cell Biology and Histology, Academic Medical Center, University of Amsterdam, Meibergdreef 15, 1105 AZ Amsterdam, The Netherlands;
[e] Department of Biological Sciences, Macquarie University, North Ryde, NSW 2109, Sydney, Australia

ABSTRACT

The nuclear lamina provides structural support to the nucleus and has a central role in defining nuclear organization. Defects in its filamentous constituents, the lamins, lead to a class of diseases collectively referred to as laminopathies. On the cellular level, lamin mutations affect the physical integrity of nuclei and nucleo-cytoskeletal interactions, resulting in increased susceptibility to mechanical stress and altered gene expression. However, little is known about the role of nuclear organization and mobility under steady-state conditions. In this study, we quantitatively compared nuclear deformation and chromatin mobility of fibroblasts from a lamin A/C-deficient patient and normal dermal fibroblasts. To this end, we created a modular toolbox in imageJ for automatically analyzing both nuclear and subnuclear dynamics in time-lapse recordings of living cells. We found that the absence of functional lamin A/C leads to increased nuclear plasticity as well as increased intranuclear mobility.

Keywords: Nuclear Dynamics, Live Cell Imaging, Shape Analysis, Tracking

1. INTRODUCTION

The lamina provides structural support to the nucleus and has a central role in defining interphase nuclear organization. Mutations in genes encoding nuclear envelope (NE) associated proteins, can elicit functional defects, which lead to a broad spectrum of nuclear envelopathies, the most striking class of which are the laminopathies[1]. This diverse cluster of diseases is caused by mutations in the LMNA gene or genes encoding proteins that affect its end products' (lamin A/C) posttranslational processing. The causative mechanisms of disease in laminopathies are not yet completely understood, but in general lamin defects alter the physical integrity of nuclei, resulting in increased susceptibility to mechanical stress and alterations in (mechanosensitive) gene expression[2]. Several lamina proteins are (in-)directly involved in chromatin organization and binding to specific DNA loci, among which the telomeres, the very ends of chromosomes[3]. Interestingly, telomeres are retained after nuclear elution procedures, giving rise to the hypothesis that these chromosomal elements are anchored to a nuclear scaffold structure[4].

To determine whether lamin A processing has an influence on telomere dynamics and nuclear dynamics in general, we visualized telomere-binding fusion proteins in patient fibroblasts using light economical imaging techniques such as controlled light exposure microscopy (CLEM)[5] and low-illumination widefield microscopy. A modular workflow was designed in ImageJ[6] for measuring nuclear deformation and individual telomere displacements through time. With this toolbox, we quantitatively compared multilevel nuclear dynamics between human fibroblasts deficient in functional lamin A/C and wild type cells. We thereby distinguished varying levels of nuclear plasticity and different regimes of telomere mobility. In this paper, we describe the dedicated image processing workflow in more detail.

2. MATERIALS AND METHODS

2.1 Workflow

ImageJ offers a wide range of basic and more advanced image processing algorithms and its functionality can easily be expanded by means of user scripting[6]. We have combined several built-in algorithms with home-written

procedures into a modular toolbox, consisting of macro sets and plugins, with custom-made verification and interaction procedures. The sequence of image processing steps is summarized in Figure 1 and discussed in more detail in the following sections.

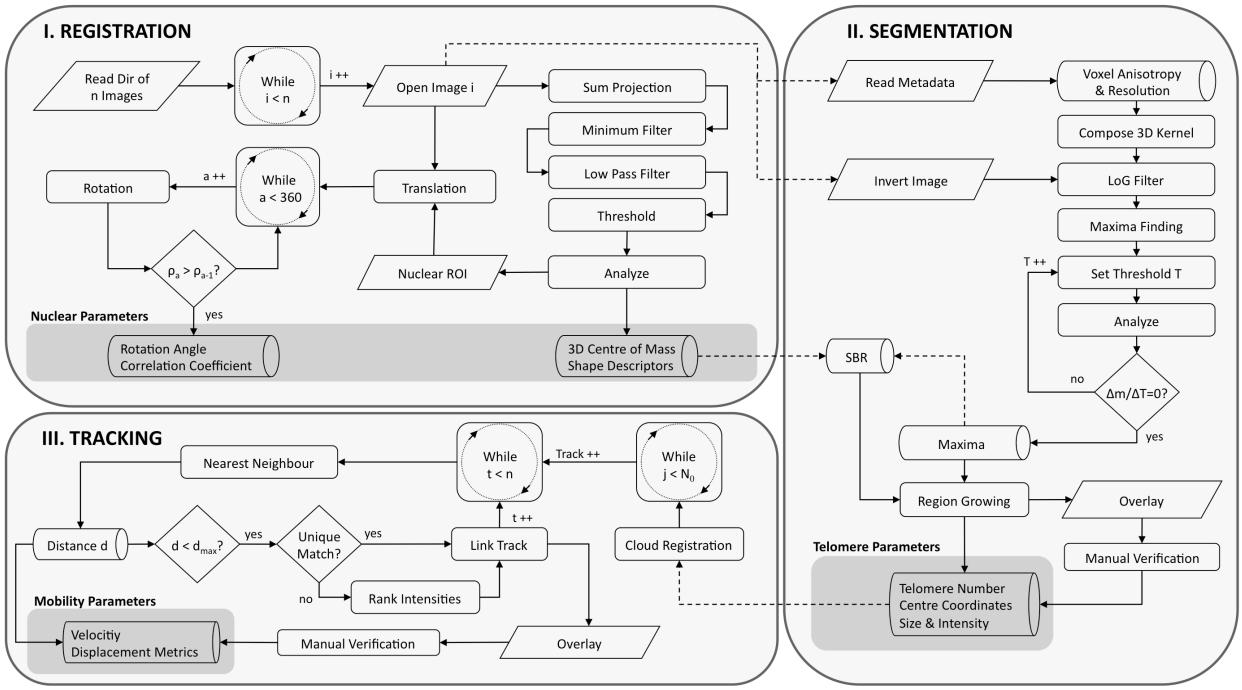

Figure 1. Flow chart of image processing steps for joint telomere mobility and nuclear deformation analysis (see text for details). Legend: a: angle, n: number of time points and image stacks, ρ: correlation coefficient, SBR: signal to nuclear background ratio, m: number of maxima, T: lower threshold setting, N_0: number of telomeres in the first time point, t: time point.

2.2 Registration

Living adherent cells show a degree of mobility that depends on the cell type, the cell cycle stage and the confluency level. Most interphase fibroblasts from normal individuals are relatively static over time, while nuclei from LMNA$^{-/-}$ can be highly mobile. Cells can move across the glass support surface, showing translational and rotational components of motion. Furthermore, long term imaging of living cells is often associated with focus drift and manual or software driven correction causes axial jumps. Accurate, unbiased tracking of subnuclear particles, such as telomeres, demands a correction for this superimposed motion by means of image registration. Cells correctly expressing mCitrine-hTRF2 typically show a punctuate pattern of telomere-localized protein within a nucleoplasmic pool of non-bound protein. Exactly this nuclear background is used for registration. This is a rigid registration, consisting of a translation and a rotation and is performed on the time point sum projections. Telomeric foci are usually far more intense than the nucleoplasmic background signal (2-5 times) and can distort the segmentation of the nuclear outline, especially those proximal to the nuclear periphery. Therefore the images are first convolved with a small minimum filter (sigma=0.3µm/r, r being the pixel size in µm). As such, moving telomeres will minimally affect this translation procedure. Subsequently, nuclear ROIs are low pass filtered (Gauss, sigma=0.75µm/r) and segmented according to the isodata autothreshold procedure. Using this nuclear mask, the three-dimensional centres of mass of all time points are determined and aligned. Next, nuclear rotation is corrected for by progressively rotating the translated images around the (now unique) centre of mass and by calculating the correlation coefficient between images of consecutive time-points. Given intensity measurements i(x,y) of the translated image at time point t, the temporal correlation ρ as a function of time lag τ is defined as:

$$\rho_{t,\tau} = \frac{\sum_{xy} \delta(x,y,t) \cdot \delta(x,y,t+\tau)}{\sqrt{\sum_{xy} \delta(x,y,t)^2 \sum_{xy} \delta(x,y,t+\tau)^2}}, \qquad (1)$$

with $\delta(x,y,t) = i(x,y,t) - \bar{i}_t$, the pixel-wise deviation from the average image intensity at time point t and τ=1. The angle at which the correlation coefficient reaches a maximum is retrieved for rotational registration. We have chosen to separate the translation and rotation step for reasons of maximal verification possibility. For instance, sometimes other nuclei enter the field of view which may perturb the correlation results. Outlining of the nucleus in the translation step allows for removing all non-target features.

2.3 Nuclear Dynamics Analysis

The primary output from the aforementioned registration procedure can simultaneously be used to generate information about the mobility characteristics of the system under investigation. For example, the correlation coefficient, described in Eq. (1), also gives a direct estimate of the allover variability in the registered time stack. Expanding the spectrum of time lags (τ) to cover the total time span produces a temporal autocorrelation curve with intrinsic statistical relevance. Likewise, the segmentation of the sum-projected images results in generation of nuclear outlines, which can be used for shape analysis. ImageJ provides many shape descriptors, such as the $circularity = 4\pi S/P^2$, by default, but other metrics were incorporated as well for detection of more subtle shape variations. The following parameters were added to the analysis[7]: $convexity = S/S(convex\ hull)$, $compactness = \frac{\sqrt{4S/\pi}}{A}$, $E_b = \frac{\sum_{i \in contour} c_i}{contour.length}$ and $curvature\ ratio = \frac{E_b(ellipsoid\ fit)}{E_b}$, with S the surface, P the perimeter, A the long half axis of the fitted ellipse, E_b the bending energy and the c_i the curvature of element i of the contour, with $c_i = \pi - \left[\arctan 2\left(\frac{y_{i+k} - y_i}{x_{i+k} - x_i}\right) - \arctan 2\left(\frac{y_i - y_{i-k}}{x_i - x_{i-k}}\right)\right]$.

2.4 Telomere Segmentation

Due to the optical imperfections of the microscope and the inherent limitations of light (diffraction), image formation is accompanied by blurring. This blurring can be mathematically described by the point spread function (PSF). Typically, the point spread function of a confocal microscope is an anisotropic function which can be approximated by a 3D Gaussian function[8]. The standard deviation of this Gaussian in the axial direction is 2 to 3 times larger than in the lateral direction, depending on the pinhole size. Consequently, small point-like objects such as telomeres will appear as elongated Gaussian-like blobs within a nuclear background. An appropriate detector for these blobs is the three-dimensional Laplace of Gaussian (LoG) operator[9], which follows the general expression:

$$LoG = f(x;\mu,\sigma_x,\sigma_y,\sigma_z) = C \cdot \left(\frac{x^2-\sigma_x^2}{\sigma_x^4} + \frac{y^2-\sigma_y^2}{\sigma_y^4} + \frac{z^2-\sigma_z^2}{\sigma_z^4}\right) \cdot \exp\left(-\frac{x^2}{2\sigma_x^2} - \frac{y^2}{2\sigma_y^2} - \frac{z^2}{2\sigma_z^2}\right), \qquad (2)$$

where C represents a constant and σ represents the standard deviation of the lateral (xy) or axial (z) dimension. The advantage of this approach is that one can tune the standard deviation and size of the kernel in each dimension separately to match the blurring imposed on the objects by the PSF. Thus, under conditions of isotropic sampling σ_z should be approximately $3\sigma_{xy}$. However, for reasons of speed and cellular viability during live cell imaging, images were sampled relatively less in z than in xy (approximately two-fold with respect to the max. obtainable resolution). To allow adequate detection of these flattened blobs we reduced the standard deviation in z by a factor 2 ($\sigma_z=\sigma_{xy}/2$).

After convolution of the inverted image with the LoG kernel, local maxima are sought. A progressive thresholding loop is initialized, until the corresponding number of maxima reaches a plateau. The scoring window is limited by a maximum number of particles, e.g. 92 for normal diploid cells and depending on the image quality the stringency of the plateau can be adjusted: in case of strong signals the derivative of the count profile is likely to become zero at a certain point whereas in noisy images, the probability of this is low and therefore, some deviation can be allowed, e.g. change by less than 5%. To establish 3D telomere identity, conditional region growing expands the selected maxima back to the particle size. The advantage of using maxima based particle extraction in comparison to direct thresholding is that this approach will allow partially overlapping and touching particles to be separated in 3D. Since region growing is dependent on the intensity of the nuclear background, we introduced a parameter for estimating spot resolvability, which reflects the ratio of the average intensity of the maxima to the median nuclear signal (signal-background ratio). In widefield recordings, analogous 2D operations are performed.

2.5 Telomere Tracking

Subsequent intensity weighted centroid determination allows telomere localization with subresolution accuracy[10]. In order to establish telomere identity from frame to frame, a nearest-neighbour criterion was used. For each telomere centre in time point t the nearest centre, in Euclidean distance, is sought in time point t+1. The region in which to look for nearest neighbours is restricted by a user-defined maximum radius. Telomere tracking is complicated by the occurrence of transient proximity effects such as fusions or collisions. Correct maintenance of telomere identity across time is therefore supported by an iterative analysis and feedback between location and telomere intensity in time. If multiple equidistant candidates exist for the same track, the intensity of the respective telomeres is brought into account, allowing extraction of the most probable corresponding telomere. A second pass eliminates doubles per time point. Doubles are candidate track telomeres in time point t+1 assigned to multiple telomeres in time point t.

Only complete tracks, which span the entire time window, are preserved; all other tracks are reset to zero. This procedure is looped until no new complete tracks are formed. Tracks can be visually verified – on orthogonal views, projections or in 4D, making use of a modified version of the Volume Viewer plugin[11] – and if necessary manually corrected. An interactive macro tool is available for deleting incorrect tracks, rerouting tracks or adding complete tracks, which have been missed by the analysis. Finally, the centres of mass of the entire telomere cloud are used for fine-tuning the registration. Extensive tests and simulations were performed to validate the robustness and accuracy of the segmentation and tracking algorithm[12].

To describe the mobility of individual telomeres different metrics are calculated: interval displacements, peak displacement (the end-to-end distance), cumulative displacement and mean square displacement (MSD), which for each time lag τ equals:

$$MSD(\tau) = \frac{1}{n-i}\sum_{i=\tau}^{n}\left(\vec{r}(t_i) - \vec{r}(t_{i-\tau})\right)^2, \qquad (3)$$

with n the total number of time points and $\vec{r}$ the n-dimensional vector of the telomere centre at time point t. A cursor-responsive macro tool allows for interrogating the mobility characteristics of individual telomeres as well.

3. RESULTS

The analysis was tested on and applied to images acquired with different light microscopy techniques (wide-field and CLEM), with or without application of restoration methods (deconvolution). Figure 2 illustrates some intermediate and output images of the joint mobility/deformation analysis on typical images acquired with CLEM.

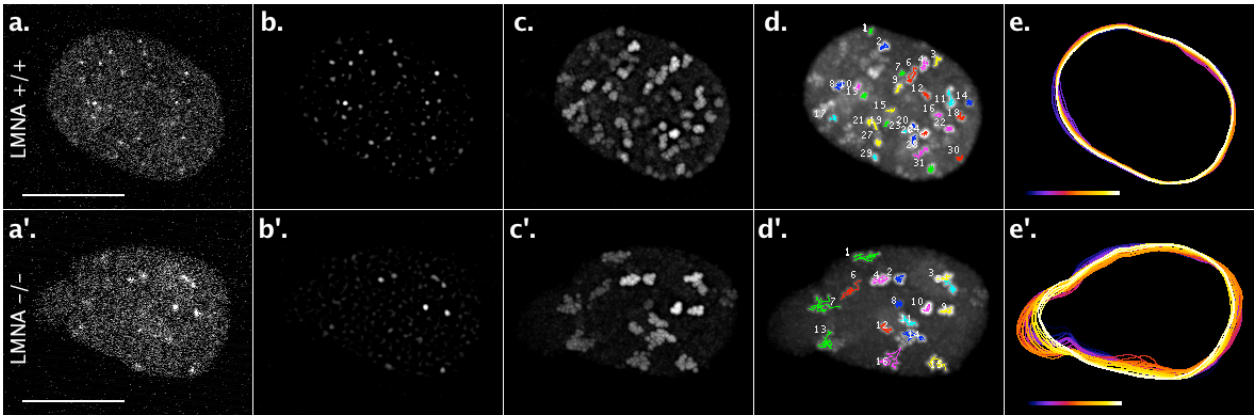

Figure 2. Example images illustrating different aspects of the analysis of nuclear dynamics on nuclei from a LMNA$^{+/+}$ (a-e) and a LMNA$^{-/-}$ (a'-e') cell. (a,a') confocal section of a CLEM image at a single time point; (b,b') the same image after LoG-mediated spot enhancement, contrast stretched; (c,c') maximum projection of LoG-filtered time stack (40 time points, 2min intervals), demonstrating telomere territories; (d,d') 2D-projected time points superimposed with the two-dimensional component of telomere tracks, retrieved by the analysis. (e,e') time-color coded projection of the two-dimensional nuclear outlines. The scale bar represents 10µm, the calibration bar represents the time (0'-80', from left to right).

To obtain a general impression of the allover dynamics in the time recordings, without explicit segmentation of any feature (nucleus nor telomere), a correlation analysis was performed. The inter-time point correlation (τ=1) was significantly more variable for LMNA$^{-/-}$ cells than for control (LMNA$^{+/+}$) cells (Fig. 3a). Likewise, the temporal autocorrelation curve of LMNA$^{-/-}$ cells showed a steep decrease with increasing time lag, whereas nuclei from LMNA$^{+/+}$ cells retained a relatively high autocorrelation throughout the recording period (Fig. 3b). These marked differences in nuclear dynamics were investigated in more detail by looking at the individual contributions of nuclear deformation and telomere mobility. We first quantified nuclear deformation in terms of shape descriptors, using the nuclear outlines from the sum projections. Fig. 3cd clearly shows that the individual profiles of nuclear circularity in LMNA$^{-/-}$ cells show extensive fluctuations through time, whereas LMNA$^{+/+}$ cells show relatively rigid profiles, also leveled at higher values.

Next, we investigated telomere mobility. On average, the tracking efficiency – the relative number of telomeres that were correctly tracked throughout the imaging period – for a 3D CLEM recording of 40 time points sampled at 2 min intervals ranged between 25% and 50%, depending on the cell type, SNR and SBR. This means the algorithm was able to retrieve a total of 15 to 30 tracks with little to no apparent incorrect assignments. For widefield recordings, the efficiency was higher (~60-80%).

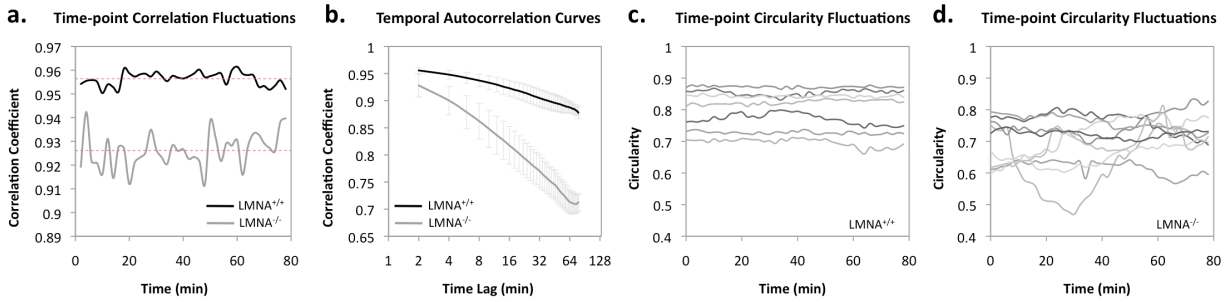

Figure 3. Nuclear deformation analysis on registered recordings of nuclei from LMNA$^{+/+}$ and LMNA$^{-/-}$ cells, transiently expressing mCitrine-hTRF2. (a) average correlation coefficient between consecutive time points per cell type (red interrupted lines indicate global time-average); (b) average temporal autocorrelation curves (±std) as a function of time lag; (c) shape deformation through time, represented by the circularity, for individual nuclei of LMNA$^{+/+}$ cells or (d) LMNA$^{-/-}$ cells.

As documented before, the overall displacement of telomeres was limited to small subnuclear volumes, which we have termed telomere territories[13]. Still, a significant difference could be observed between the two cell types. The maximal peak displacement for instance, for LMNA$^{+/+}$ and LMNA$^{-/-}$ cells was 3.1µm and 6.9µm, respectively (see also Fig. 4a). Whereas MSD plots of normal fibroblasts (LMNA$^{+/+}$) were characterized by a plateau, typical of constrained diffusive motion, several LMNA$^{-/-}$ cells displayed MSD plots that lacked a clear plateau within the time intervals studied, often but not always due to a fraction of telomeres showing distinct directed motion (Fig. 4b).

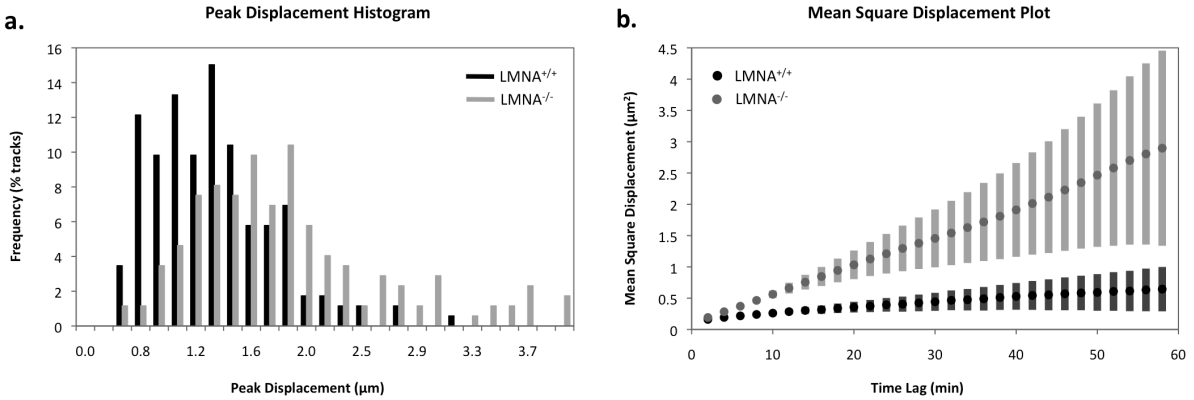

Figure 4. Telomere Mobility analysis on registered recordings of nuclei from LMNA$^{+/+}$ and LMNA$^{-/-}$ cells, transiently expressing mCitrine-hTRF2. (a) Histogram of peak displacements of all tracks in both cell types (the x-axis was clipped for ease of interpretation); (b) Average mean square displacement plots (±stdev) for both cell types. Pooled data from ±10 nuclei.

4. CONCLUSIONS

We have established a workflow in ImageJ for analyzing nuclear dynamics on multiple levels. This allowed quantifying nuclear deformation and telomere mobility in fibroblasts from humans with a different disease state, thereby demonstrating significant differences. For the analysis of telomere mobility throughout time, we removed nuclear motion and drift in the images using a rigid registration (nuclear translation and rotation) followed by a fine-tuning based on the telomere cloud. However, cells sometimes roll or – as in the case of LMNA$^{-/-}$ cells – deform. In such instances this approach becomes limiting and integrative three dimensional pattern-based registration procedures need to be implemented. To address rolling phenomena we have elaborated on the matching pairs support algorithm – which is based on the principle of finding a pair of points between two time frames for which a maximum support of equidistant pairs can be found[14] – but found little differences in tracking results for these cells, as they are quite flat and mostly move in the lateral plane. In addition, this approach still does not cover for deformation, which can impose a significant bias on the interpretation of telomere mobility results. Indeed, telomere mobility in LMNA$^{-/-}$ cells can be overestimated or misinterpreted (for intrinsic mobility) as it is partially governed by the higher-level nuclear deformation. On the other hand, increased telomere mobility was also observed in LMNA$^{-/-}$ cells that were devoid of any dramatic shape changes and also on the millisecond level, a time scale in which the influence of these large deformations can be neglected[15]. This supports the biological relevance of our

findings. Nevertheless, to allow more accurate quantification of telomere mobility in deformable nuclei we are currently looking into methods for affine registration such as contour mapping[16].

Another aspect for improvement is the tracking efficiency, which was currently limited to about 50% and was inversely correlated with the duration of the recording, the sampling interval, and the frequency of telomere collisions. The absolute number of tracks retrieved can be increased to some extent by enlarging the maximum allowable displacement per time step, but this will result in a higher risk of false track assignment. Another option would be to perform time-point binning in order to recover track consistency for telomeres that are not detected in a single time point, because of intensity fluctuations or a fusion/collision event. On the other hand, such an approach reduces spatiotemporal resolving power and could lead to creation of artifacts by fast moving telomeres. In the current set-up, fusing and separating particles will result in loss of one track, since only the best corresponding object, based on intensity correspondence, is retained. In theory, these events result in intensity and volume shifts that should allow recognition[8], but inclusion of such criteria was not considered in our algorithm because of the relatively high basal intensity fluctuations of individual telomeres.

In spite of its current limitations, the depicted analysis performed well on images with varying quality and biological content and revealed novel insights in the biology of laminopathies. With minor modifications and better integration, this workflow can have generic relevance for different cell biological research topics.

ACKNOWLEDGEMENTS

The Hercules Foundation is gratefully acknowledged.

REFERENCES

1. J. L. Broers, F. C. Ramaekers, G. Bonne, R. B. Yaou and C. J. Hutchison, “Nuclear lamins: laminopathies and their role in premature ageing”, *Physiol Rev.* **86**, pp. 967-1008, 2006.
2. K. N. Dahl, A. J. Ribeiro, and J. Lammerding, “Nuclear shape, mechanics, and mechanotransduction”, *Circ.Res.* **102**, pp. 1307-1318, 2008.
3. T. Dechat, A. Gajewski, B. Korbei, D. Gerlich, N. Daigle, T. Haraguchi, K. Furukawa, J. Ellenberg and R. Foisner, “LAP2alpha and BAF transiently localize to telomeres and specific regions on chromatin during nuclear assembly”, *J.Cell Sci.* **117**, pp. 6117-6128, 2004.
4. T. de Lange, “Human telomeres are attached to the nuclear matrix”, *EMBO J.* **11**, pp. 717-724, 1992.
5. R. A. Hoebe, C. H. Van Oven, T. W. Gadella, P. B. Dhonukshe, C. J. Van Noorden and E. M. M. Manders, “Controlled light-exposure microscopy reduces photobleaching and phototoxicity in fluorescence live-cell imaging”, *Nat.Biotechnol.* **25**, pp. 249-253, 2007.
6. W. S. Rasband, ImageJ, N.I.H., Bethesda, Maryland, USA, http://rsb.info.nih.gov/ij/, 1997-2009.
7. J. C. Russ, The image processing handbook, CRC/Taylor & Francis, Boca Raton, FL, 2007.
8. C. B. Bergsma, G. J. Streekstra, A. W. Smeulders and E. M. M. Manders, “Velocity estimation of spots in three-dimensional confocal image sequences of living cells”, *Cytometry* **43**, pp. 261-272, 2001.
9. D. Sage, F. R. Neumann, F. Hediger, S. M. Gasserand and M. Unser, “Automatic tracking of individual fluorescence particles: application to the study of chromosome dynamics”, *IEEE Trans Image Process* **14**, pp. 1372-1383, 2005.
10. E. M. M. Manders, R. A. Hoebe, J. Strackee, A. M. Vossepoel and J. A. Aten, “Largest contour segmentation: a tool for the localization of spots in confocal images”, *Cytometry* **23**, pp. 15-21, 1996.
11. K. U. Barthel, http://rsb.info.nih.gov/ij/plugins/volume-viewer.html, 2005.
12. W. H. De Vos, G. H. Joss, W. Haffmans, R. A. Hoebe, E. M. M. Manders and P. Van Oostveldt, “Four-dimensional telomere analysis in recordings of living human cells acquired with Controlled Light Exposure Microscopy”, *J. Microsc.* **238**, pp. 254-264 (2009).
13. W. H. De Vos, R. A. Hoebe, G. H. Joss, W. Haffmans, S. Baatout, P. Van Oostveldt and E. M. M. Manders, “Controlled light exposure microscopy reveals dynamic telomere microterritories throughout the cell cycle”, *Cytometry* **75**, pp. 428-439, 2009.
14. P. Matula, M. Kozubek and V. Dvorak, “Fast point-based 3-D alignment of live cells”, *IEEE Trans.Image Process* **15**, pp. 2388-2396, 2006.
15. W. H. De Vos, F. Houben, R. .A. Hoebe, R. Hennekam, B. Van Engelen, E. M. M. Manders, F. C. Ramaekers, J. L. Broers and P. Van Oostveldt, “Increased plasticity of the nuclear envelope and hypermobility of telomeres due to the loss of a-type lamins”, *Biochim Biophys Acta* **1800**, pp. 448-458, 2010.
16. J. De Vylder, K. Douterloigne, W. H. De Vos and W. Philips, “2D mapping of strongly deformed cell nuclei based on contour warping”, IEEE 32nd Annual International Conference of the IEEE Engineering in Medicine and Biology Society (EMBC'10), 2010.